INORGANIC CHEMISTRY FRONTIERS

RESEARCH ARTICLE

View Article Online
View Journal



Cite this: DOI: 10.1039/d5qi02274f

# Polycyclic aromatic hydrocarbon chromophores tune photo-physical properties in bichromophoric Cu(I) photosensitizers

Oliver Lange, †[a] Florian Doettinger, †[a,b] Lars E. Burmeister, [a] Johannes P. Zurwellen, [a] Toni M. Maier, [c] Christian Kleeberg, [d] Michael Karnahl, [a] Christoph R. Jacob *[c] and Stefanie Tschierlei *[a]

A modular design approach for bichromophoric Cu(I) complexes is reported, combining a [Cu(N^N)(P^P)]$^+$ scaffold that supports metal-to-ligand charge transfer with two polycyclic aromatic hydrocarbon chromophores covalently attached to the diimine ligand. Three new systems incorporating 9,9-dimethyl-9*H*-fluorene, phenanthrene, and anthracene units at the 4,7-positions of neocuproine were synthesized and fully characterized. Structural analysis reveals twisted geometries of the attached chromophores, which reduce conjugation with the diimine core. Electrochemical measurements indicate only moderate shifts in reduction potentials, indicating preservation of the Cu(I)-centered redox behavior. Across the series, the visible MLCT band is retained without pronounced red-shifts, while the molar attenuation coefficients increase markedly (×1.7–3.4 *vs.* the reference), in line with calculated oscillator strengths. Fragment comparisons and computations attribute the additional UV intensity to intraligand charge transfer (9,9-dimethyl-9*H*-fluorene, phenanthrene) and to vibronically structured $\pi_A^* \leftarrow \pi_A$ transitions (anthracene), consistent with the non-coplanar geometries. Complexes bearing 9,9-dimethyl-9*H*-fluorene and phenanthrene substituents exhibit yellow emission involving the Cu(I)-based metal-to-ligand charge transfer state ($\lambda_{em} \approx 565$ nm, $\tau$ up to 20.8 μs), whereas the anthracene-substituted system populates a non-emissive $^3\pi$–$\pi^*$ triplet state localized on an anthracene moiety ($\tau > 35$ μs), as evidenced by transient absorption spectroscopy and time-dependent density functional theory. These results establish clear structure–property relationships in bichromophoric Cu(I) systems and illustrate how polycyclic aromatic hydrocarbon chromophores influence excited-state character and dynamics.

Received 8th November 2025,
Accepted 5th January 2026

DOI: 10.1039/d5qi02274f

rsc.li/frontiers-inorganic



## Introduction

The class of heteroleptic Cu(I) complexes has experienced a rise in popularity due to their diverse and successful applications in the field of photochemistry, including photoredox catalysis,[1–3] dye-sensitized solar cells (DSSCs),[4–7] light-emitting diodes[8,9] or solar fuels production.[10–16] In comparison to established and commercially available standards such as Ru(II) or Ir(III) complexes,[17–19] the attractiveness of Cu(I)-based photosensitizers (CuPSs) can be attributed to different factors: (i) the significantly lower cost of copper due to its much higher abundance in the Earth's crust (Cu: 27 ppm *vs.* Ru: $37 \times 10^{-6}$ ppm),[20,21] (ii) the $d^{10}$ shell, which prevents low-energy metal-centered (MC) states that can cause undesirably rapid excited-state deactivation, and (iii) the potential to outperform their noble-metal competitors.[1,10,22,23] Numerous studies have already demonstrated that noble-metal-free systems for the reduction of water or carbon dioxide can be achieved using a heteroleptic CuPS along with a suitable earth-abundant-metal catalyst (*e.g.* based on Fe or Mn).[11,14,24–27] Thus, further research and development of improved CuPSs can contribute to a more sustainable conversion of solar energy.

In general, heteroleptic CuPSs of the type [Cu(N^N)(P^P)]$^+$ combine a diimine (N^N) and diphosphine (P^P) ligand that can both be tuned separately. The diimine ligand, *e.g.* neocuproine (2,9-dimethyl-1,10-phenanthroline, **neo**), has strong π-accepting properties that allow for the formation of low-lying

[a]*Department of Energy Conversion, Institute of Physical and Theoretical Chemistry, Technische Universität Braunschweig, Rebenring 31, 38106 Braunschweig, Germany. E-mail: s.tschierlei@tu-bs.de*
[b]*Department of Chemistry, University of Basel, St Johanns-Ring 19, CH-4056 Basel, Switzerland*
[c]*Institute of Physical and Theoretical Chemistry, Technische Universität Braunschweig, Gaußstraße 17, 38106 Braunschweig, Germany. E-mail: c.jacob@tu-braunschweig.de*
[d]*Institute of Inorganic and Analytical Chemistry, Technische Universität Braunschweig, Hagenring 30, 38106 Braunschweig, Germany*
† These authors share the first authorship of this paper.

excited metal-to-ligand charge transfer (MLCT) states.[28] Hence, the diimine ligand is typically modified to alter the photophysical properties of the CuPS.[3,29,30] One strategy to improve the relevant MLCT states, *i.e.* absorptivity and lifetime, is to attach an additional organic chromophore to the diimine to create a bichromophoric system.[31–40] The attachment of the chromophore can be achieved *via* a single covalent bond with or without a linking group. The variety of linker groups is large and some common examples include alkyl, phenyl, triazole, thiophenyl, or alkynyl moieties.[33,41–44] Moreover, the use of linking groups adds another dimension to the ligand design, because each bridge has its own properties *e.g.* rigidity and size.[41,44,45] The advantages of combining chromophores can be numerous: (i) increased absorptivity (antenna effect), (ii) potential red-shifted absorption through π-conjugation, (iii) exploitation of high spin–orbit coupling on the sensitizer for efficient triplet generation and low spin–orbit coupling for the stabilization of long-lived triplet states on the organic chromophore, (iv) individual tunability, and (v) prolonged excited-state lifetimes through the reservoir effect.[34–36,45–47] The latter is particularly attractive as the excited-state lifetime is a crucial factor for photocatalytic applications.[48,49] However, synthesizing and analyzing such bichromophoric systems can be challenging and typically requires an interdisciplinary approach.

In a previous study, Doettinger *et al.* revealed by steady-state and time-resolved spectroscopy together with quantum-chemical computations that additional pyrene chromophores act as an energy sink for CuPS MLCT states.[50] This concept enabled efficient singlet oxygen sensitization, with yields depending on the position (4,7 *vs.* 5,6) where the pyrene was attached to the **neo** ligand.[50] In another study, Takeda *et al.* attached a variety of phenyl, thiophenyl and furan units to the 4,7-positions of **neo**.[15] Most complexes retained their MLCT behavior, but heterocycles bearing a heteroatom in 2-position displayed altered excited states and reactivities.[15]

To expand the catalog of diimines and bichromophoric systems, three new ligands were developed in this study (Fig. 1) in which the 4,7-positions of **neo** are symmetrically disubstituted with polycyclic aromatic hydrocarbon (PAH) chromophores: 9,9-dimethyl-9*H*-fluorene (**F**), phenanthrene (**P**) and anthracene (**A**). To suppress potential deactivation channels, *e.g.* through n–π* states, heteroatoms were avoided in the substituents. According to the El-Sayed rule, these states allow higher crossing rates between systems.[28,51] Furthermore, **F**, **P** and **A** are rigid and modifiable chromophores with well-defined absorption characteristics and sufficient photostability.[52–58] For these reasons, they were used in diverse applications including fluorescence microscopy dyes,[58] dye lasers,[59] DSSCs,[60] two-photon absorption[59,61] and photon upconversion.[54,57,62,63]

While PAHs have many desirable applications, this work focuses on the synthesis and in-depth characterization of the novel **neo** derivatives 4,7-bis(9,9-dimethyl-9*H*-fluoren-2-yl)-neocuproine (**nF**), 4,7-di(phenanthren-9-yl)-neocuproine (**nP**), 4,7-di(anthracen-2-yl)-neocuproine (**nA**) and their respective heteroleptic Cu(I) complexes **CunF**, **CunP**, and **CunA** (Fig. 1, P^P: xantphos, anion: $PF_6^-$). As references, **neo** and bathocuproine (**bcp**) as well as the complexes **Cuneo** and **Cubcp** were selected.

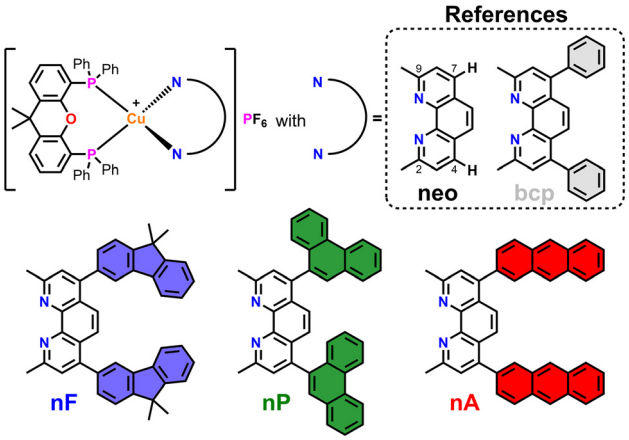


**Fig. 1** Schematic representation of the diimine ligands and their respective heteroleptic Cu(I) complexes investigated in this study. The influence of different PAH chromophores (**F** = 9,9-dimethyl-9*H*-fluorene, **P** = phenanthrene, **A** = anthracene) on key photophysical and electrochemical properties is assessed. **neo** = neocuproine, also 2,9-dimethyl-1,10-phenanthroline, **bcp** = bathocuproine, also 2,9-dimethyl-4,7-diphenyl-1,10-phenanthroline, **nF** = 4,7-di-(9,9-dimethyl-9*H*-fluoren-2-yl)-2,9-dimethyl-1,10-phenanthroline, **nP** = 2,9-dimethyl-4,7-di(phenanthren-9-yl)-1,10-phenanthroline and **nA** = 4,7-di(anthracen-2-yl)-2,9-dimethyl-1,10-phenanthroline.

The following sections present structural, electrochemical and spectroscopic analysis supported by density functional theory (DFT) and time-dependent DFT (TDDFT) calculations, providing insights into the interplay between the different chromophores.

## Results and discussion

### Synthesis

The reference ligands **neo** and **bcp** were acquired commercially. The syntheses of the three novel ligands **nF**, **nP** and **nA** were conducted *via* Suzuki–Miyaura cross-coupling reactions[64,65] from the common substrate 4,7-dichloro-2,9-dimethyl-1,10-phenanthroline[66] and their corresponding boronic acids (for **nF**: 9,9-dimethyl-9*H*-fluoren-2-yl-2-boronic acid, for **nP**: phenanthrene-9-boronic acid, for **nA**: anthracene-2-boronic acid; further details see SI Chapter 2). The precursor 4,7-dichloro-2,9-dimethyl-1,10-phenanthroline was synthesized on gram-scale as described elsewhere.[65,66] Subsequent cross-coupling reactions were conducted in a THF/water mixture using $K_3PO_4$ as base (0.5 M aqueous solution). To ensure efficient cross coupling, the XPhos-Pd-G2 precatalyst was employed, which under basic conditions releases a highly reactive XPhos-$Pd^0$ species.[67] Compared to the more commonly used [$Pd(PPh_3)_4$], the XPhos-Pd-G2 precatalyst is often a more convenient and reliable choice for transformations involving 4,7-dichloro- or 5,6-dibromo-1,10-phenanthroline derivatives, as shown in earlier studies.[23,50,65] The target ligands **nF**, **nP**

and **nA** were obtained after column chromatography on basic aluminum oxide in yields of 91%, 77% and 80%, respectively (for further details SI Chapter 2, 3 and 4).

The complexes were synthesized *via* a well-established two-step, one-pot approach,[10,68,69] in which the xantphos ligand is first coordinated to the Cu(I) precursor $[Cu(CH_3CN)_4]PF_6$ in deaerated dichloromethane at elevated temperatures (SI Chapter 2). Subsequently, the respective diimine ligand (**nF**, **nP** or **nA**) was added dropwise at 0 °C for at least one hour using an automatic syringe pump. Adding the reagent at low temperature prevents formation of the thermodynamically favored homoleptic $[Cu(N\hat{}N)_2]PF_6$ side product.[3,70–73] Typically, isolation of the complexes proceeds *via* slow precipitation using *n*-hexane to afford crystalline solids. However, due to the bulky π-extended chromophores, the complexes synthesized herein formed deep red oils rather than solids upon *n*-hexane addition. This behavior was also observed for pyrenyl-substituted analogs and is likely caused by competing intermolecular π–π-interactions hindering crystal formation.[50] Nevertheless, the target complexes **CunF**, **CunP** and **CunA** were successfully obtained in yields of 66%, 59% and 50%, respectively (see SI Chapter 2).

The identities and purities of all ligands and complexes were confirmed by nuclear magnetic resonance (NMR: $^1H$, $^{13}C\{^1H\}$, DEPT 135, and $^{31}P\{^1H\}$, see SI Chapter 3) and electrospray ionization high-resolution mass spectrometry (ESI-HRMS, SI Chapter 4). **nP** exhibited distinct behavior in the $^1H$ NMR spectrum, revealing an unexpected pair of singlets for the methyl protons (3.08 ppm, $\Delta$ = 0.002 ppm), whereas a single singlet is typically observed. Combined with duplicate signals in the aromatic region of the $^{13}C\{^1H\}$ and DEPT135 spectra, this strongly suggests the presence of stereoisomers. This phenomenon is also observed for **CunP**, but is absent in all other ligands or complexes. However, due to the minor structural differences and the absence of distinctive spectroscopic or electrochemical effects, the presence of these isomers was considered negligible for further discussions.

## Structural characterization

To elucidate the main structural similarities and differences between the designed complexes, DFT calculations were performed and the predicted molecular structures were analyzed. Additionally, single crystals of a solvate of **CunA** were obtained by slow diffusion of *n*-hexane into a concentrated dichloromethane/diethyl ether solution at room temperature, enabling a direct comparison between the experimental solid-state structure and the calculated geometry (Table 1, for experimental details: SI Chapter 5). The experimental (Fig. 2) and computed molecular structures (Fig. S5.1 and S5.2) are in good agreement and consistent with previous reports on heteroleptic Cu(I) complexes.[15,16,29,50,65,74] Cu–N bond lengths (206.5–212.3 pm) are consistently shorter than Cu–P bond lengths (224.3–232.6 pm), and bite angles fall within expected pseudo-tetrahedral geometry ranges (N–Cu–N: 78.3–80.4°; P–Cu–P: 116.5–119.7°). The interplane angles $\theta$ between the planes formed by the N–Cu–N and P–Cu–P atoms (83.2–87.7°) are typical for such heteroleptic Cu(I) complexes.[15,16,29,50,65,75,76]

In general, the geometry around the central Cu(I) atom is largely unaffected by the substituents, which is reasonable as the 4,7-positions are *para* to the copper-binding nitrogens. The $C_4$–$C_{Sub1,1}$ and $C_7$–$C_{Sub2,1}$ bond lengths (Table 1) confirm a carbon–carbon C–C single bond, with average values of 149.2 pm (exp.) and 147.7 pm (calc.). The observed torsion angles $\vartheta_{sub1,2}$ along atoms $C_3$–$C_4$–$C_{Sub1,1}$–$C_{Sub1,2}$ and $C_8$–$C_7$–$C_{Sub2,1}$–$C_{Sub2,2}$ resemble those of biphenyl-like systems ($\vartheta_{solid}$ = 0–10°, $\vartheta_{vapor}$ = 44.4 ± 1.2°, $\theta_{solute}$ = 30–40°), where conjugation ($\vartheta \approx 0°$) and steric hindrance ($\vartheta \approx 90°$) compete.[77–80] For the present series, the effective torsion between the **neo** plane and the substituent plane is 50.2–57.7° for **Cubcp**, **CunF**, and **CunA**, *i.e.* moderate twisting and partial conjugation limited by steric hindrance. This is primarily due to the repulsion between the *ortho*-hydrogens and the 5,6-hydrogens of the **neo** backbone, as also noted by Takeda *et al.*[81]

**Table 1** Selected bond lengths (pm), bond angles (°), N–Cu–N and P–Cu–P interplane angle $\theta$ (°) and torsion angles $\vartheta$ (°) from DFT (calc.) and X-ray (exp.) data for all complexes. The $C_{neo}$–$C_{sub}$ bond lengths describe the bond length between the respective substituent and the $C_4/C_7$ of **neo**. Torsion angles $\vartheta_{sub1}$ and $\vartheta_{sub2}$ express torsion angles along the substituent linkages from $C_3$–$C_4$–$C_{Sub1,1}$–$C_{Sub1,2}$ and $C_8$–$C_7$–$C_{Sub2,1}$–$C_{Sub2,2}$, where the second substituent carbon atom is on the same side as the stacking phenyl ring. **Cubcp** and **CunA** were analyzed both experimentally and computationally for validation (experimental data for **Cubcp** taken from ref. 16). Standard deviations are given in parentheses. Calculations at PBE0/def2-TZVP level (CPCM: $CH_2Cl_2$)

| | | **Cuneo**$_{calc.}$ | **Cubcp**$_{exp.}$ | **Cubcp**$_{calc.}$ | **CunF**$_{calc.}$ | **CunP**$_{calc.}$ | **CunA**$_{exp.}$ | **CunA**$_{calc.}$ |
|---|---|---|---|---|---|---|---|---|
| Cu–N1 | (pm) | 210.9 | 207.26(19) | 210.3 | 210.7 | 211.5 | 210.62(33) | 211.5 |
| Cu–N2 | | 212.3 | 209.63(19) | 211.4 | 211.1 | 211.1 | 211.14(38) | 210.3 |
| Cu–P1 | | 226.3 | 223.99(6) | 226.0 | 226.3 | 226.7 | 226.29(13) | 225.5 |
| Cu–P2 | | 229.6 | 230.19(6) | 229.9 | 229.2 | 229.1 | 231.68(12) | 232.6 |
| $C_4$–$C_{sub1}$ | | — | 147.5(3) | 147.6 | 147.4 | 148.1 | 149.16(61) | 147.3 |
| $C_7$–$C_{sub2}$ | | — | 148.4(3) | 147.6 | 147.5 | 148.1 | 149.77(65) | 147.4 |
| N–Cu–N | (°) | 79.7 | 80.41(7) | 79.2 | 79.2 | 79.4 | 78.253(142) | 79.0 |
| P–Cu–P | | 118.5 | 119.95(2) | 118.7 | 118.8 | 119.0 | 116.789(47) | 116.5 |
| $\theta$ | | 85.4 | 85.280(6) | 85.2 | 86.7 | 87.7 | 86.695(99) | 83.8 |
| $\vartheta_{sub1}$ | | — | −129.414(246) | −122.3 | −125.6 | −82.4 | 50.330(613) | −126.5 |
| $\vartheta_{sub2}$ | | — | 124.560(278) | 55.0 | 55.1 | 104.6 | 50.183(618) | 127.1 |

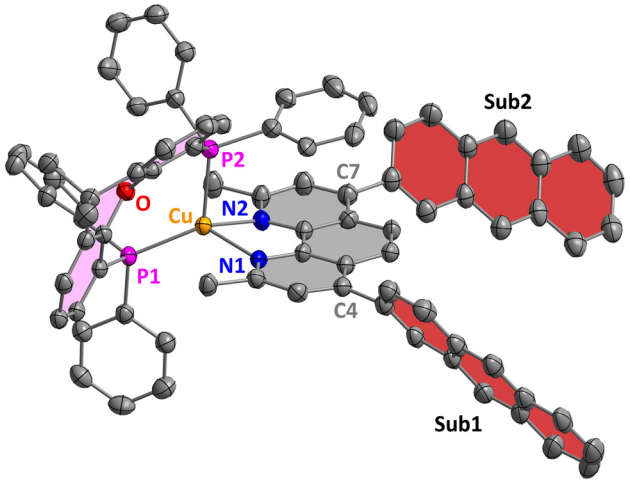


**Fig. 2** Molecular crystal structure of **CunA**. Nitrogen atoms are depicted in blue, oxygen in red, phosphorus in pink, copper in orange, and hydrogen as well as solvent molecules are omitted for clarity. The carbon atoms in 4,7-position are labeled with $C_4$ and $C_7$. Torsion angles $\vartheta$ are measured along $C_3$–$C_4$–$C_{Sub1,1}$–$C_{Sub1,2}$ and $C_8$–$C_7$–$C_{Sub2,1}$–$C_{Sub2,2}$. The second substituent $C_{Sub-2}$ is on the same side as the stacking phenyl ring.

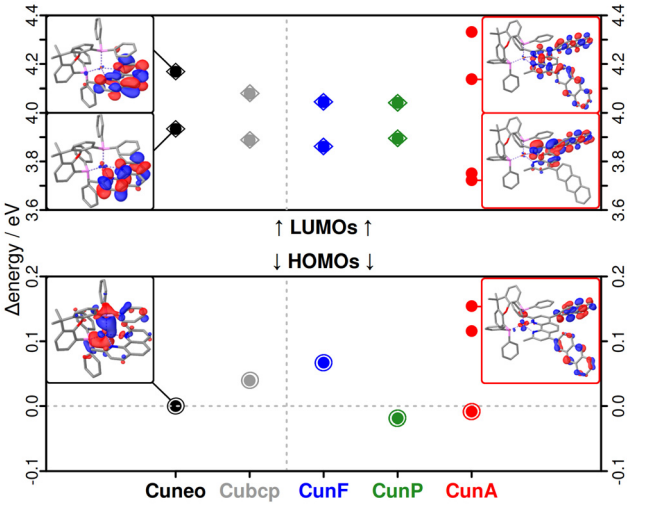


**Fig. 3** Molecular orbital energy diagram calculated with PBE0/def2-TZVP. Energy differences are given relative to the **Cuneo** HOMO (−6.15 eV) for the respective molecule columns (in eV). Encircled markers denote the $d_{Cu}$-HOMO, diamonds denote the $\pi_{neo}$*-LUMOs. Representative molecular orbitals of the latter are shown on the lefthand side for **Cuneo**, while the HOMO, LUMO and LUMO+2 of **CunA** are shown on the righthand side.

In contrast, with $\vartheta_{sub1,2}$ = 82.4 and 75.4° the phenanthrene units in **CunP** are nearly perpendicular to the diimine plane. This can be explained by the repulsion between the *ortho*-hydrogen and the adjacent methine bridge with the 5,6-hydrogen atoms of **neo**. As a result, through-bond electronic communication between **neo** and phenanthrene in **CunP** is significantly reduced, because the π-systems and p-orbitals cannot effectively overlap. Overall, torsion increases in the following order: **Cubcp** ≈ **CunF** ≈ **CunA** (50.2–57.7°) < **CunP** (75.4–82.4°) and the expected π-communication follows: **Cubcp** ≈ **CunF** ≈ **CunA** > **CunP**.

## Molecular orbital trends

To better understand the electronic communication and redox behavior, the molecular orbitals (MO) of the Cu(I) complexes (Fig. 3 and SI Chapter 6) were investigated (PBE0/def2-TZVP, CPCM: dichloromethane). The frontier molecular orbitals of **Cuneo** and **Cubcp** (Fig. S6.12 and S6.14) serve as reference systems: their highest occupied molecular orbital (HOMO) is predominantly $d_{Cu}$- and $p_P$-based, and the lowest unoccupied molecular orbital (LUMO) corresponds to a $\pi_{neo}$* orbital on the **neo** ligand, consistent with literature.[73,75,76,82–84]

The HOMO (SI Chapter 6) is only marginally affected (<0.1 eV) upon 4,7-disubstitution of **neo**, and spin density analysis of the singly-reduced species (Fig. S6.22) corroborate a neo-centered LUMO. **CunP** and **CunF** retain $\pi_{neo}$* LUMOs (Fig. S6.16 and S6.18) comparable in energy and character to the references **Cuneo** and **Cubcp** (Fig. 3, S6.12 and S6.14), reflecting minimal substituent contribution to $\pi_{neo}$*-MOs (SI Chapter 6).

Rather than forming one uniform π-system, the MOs of **neo** and the substituents (phenyl in **bcp**, phenanthrene in **nP** and 9,9-dimethyl-9*H*-fluorene in **nF**) remain largely separate. This is consistent with the non-coplanar geometries (see above) and an energetic mismatch between the π-systems. The substituent orbitals of the latter are outside the shown frontier orbital window (Fig. 3). These findings highlight the bichromophoric nature of **CunF** and **CunP**, where electronic independence of the two chromophores is largely preserved. A similar separation is observed for the ligands (SI Chapter 6). Such behavior has also been observed for related systems containing carbazole, aniline or pyrene substituents.[13,50,85]

In contrast, **CunA** displays a unique MO behavior. Four additional MOs appear within the frontier orbital region, differentiating it from the other complexes (Fig. 3). Their assignment is complicated due to the energetically close MO energies of anthracene and **neo** as well as the torsion between the anthracene and diimine units, allowing some electronic interaction. The two highest occupied MOs (HOMO, HOMO−1) lie above the $d_{Cu}$ MO (HOMO−2) and are clearly anthracene-centered (Fig. S6.20). The LUMOs, however, cannot unambiguously be assigned to either **neo** or **A** (Fig. S6.20). Thus, **CunA** differs from the other complexes in possessing notable LUMO stabilization and partial delocalization across both fragments, consistent with its distinct excited-state behavior discussed below.

## Electrochemical behavior

Cyclic voltammetry (CV) was performed to evaluate the redox behavior and support the previously discussed MO assignments. For the unsubstituted complex **Cuneo** (Fig. S7.9), a reversible one-electron reduction is observed at −2.09 V *vs.* $Fc/Fc^+$ in deaerated dimethylformamide (see Table 2).[11,50,69] The

Table 2 Reduction potentials of the substituents, ligands and complexes measured in deaerated dimethylformamide and referenced against the ferrocene/ferrocenium couple ($Fc/Fc^+$). All irreversible events are simply listed at their peak (minimum) current without special notation. Reversible signals are given as the half wave potential ($E_{red,1/2}$)

| | — | — | **F** | **P** | **A** |
|---|---|---|---|---|---|
| $E_{red}$/V | — | — | −3.13[b] | −2.73<br>−2.91[b] | −2.41[b] |
| | **neo** | **bcp** | **nF** | **nP** | **nA** |
| $E_{red}$/V | *ca.*<br>−2.7[a] | −2.60 | −2.42<br>−2.46<br>−2.70<br>−2.76 | −2.46<br>−2.53<br>−2.75 | −2.23[b]<br>−2.68 |
| | **Cuneo** | **Cubcp** | **CunF** | **CunP** | **CunA** |
| $E_{red}$/V | −2.09[b]<br>−2.83 | −2.01[b]<br>−2.63 | −1.99[b]<br>−2.47[b]<br>−2.86<br>−2.94 | −2.00[b]<br>−2.67<br>−2.76 | −1.94[b]<br>−2.25<br>−2.50<br>−2.70 |

[a] No distinct minimum determinable. [b] reversible.

localization of the reduction at the **neo** ligand was confirmed by spin density analysis of the singly reduced species (Fig. S6.22). Oxidative events were not analyzed in detail, as oxidation in heteroleptic Cu(I) complexes typically leads to irreversible cleavage of the Cu–P bond at ≈0.9 V *vs.* $Fc/Fc^+$.[23,24,86–88]

The introduction of PAH chromophores at the 4,7-positions of **neo** leads to a slight anodic shift in the reduction potential (Table 2). For **Cubcp**, a small shift to −2.01 V ($\Delta$ = +80 mV) is observed (Fig. S7.10), in line with the computations (Table S6.11). For **CunF** and **CunP**, the reduction waves are shifted by ≈ +100 mV (Table 2 and Fig. S7.11, S7.12) and correspond to the same **neo**-centered reduction. The computed shift for **CunF** (+80 mV) matches well with the experiment, while the shift for **CunP** (+40 mV) is underestimated, likely due to the lack of computed contribution from the phenanthrene unit (Fig. S6.22).

**CunA** exhibits a more complex reduction behavior, with multiple reductions between −1.9 V and −2.7 V (Fig. S7.13). A comparison with related systems and its ligand **nA** (Fig. S7.8) suggests that the reduction at −1.94 V corresponds to the **neo** based reduction ($\Delta$ = +150 mV *vs.* **Cuneo**). The calculated shift ($\Delta$ = +230 mV) is overestimated due to strong orbital contributions from anthracene, but the overall trend is reproduced. Furthermore, **CunA** has two weaker reversible reductions around −1.8 V and −1.2 V, which are also present in **nA** (Fig. S7.8), but not in **A** itself (Fig. S7.3). These features were not predicted by DFT in the present setup and may arise from intermolecular and solvent interactions or side reactions.

In summary, the observed anodic shifts in **neo**-based reductions correlate with the size of the attached π-system ($\Delta$ ≈ +100 mV for **F** and **P**, +150 mV for **A**), but remain modest overall. This supports the concept that the Cu(I) redox core is largely decoupled from the chromophoric PAH substituents. The calculated reduction potentials follow the same trend (see SI Table S6.11). The disagreement with experiment likely arises from the minimal orbital overlap in **CunP** and significant orbital mixing in **CunA** (Fig. S6.22).

## UV/vis absorption

To explore the bichromophoric character of the novel complexes, UV/vis absorption spectra were recorded. Substitution at the 4,7-positions of **neo** with PAH chromophores results in only small red-shifts, but a drastic increase in molar attenuation coefficients (Fig. 4 and Table 3). This trend has also been observed for related substitution patterns.[3,12,89]

All complexes exhibit a broad, structureless MLCT band between 350–450 nm, with $\varepsilon \approx 3–15 \times 10^3$ $M^{-1}$ $cm^{-1}$. This assignment is supported by: (i) previous reports about **Cuneo**, **Cubcp** and related complexes,[29,71,87,90,92] (ii) TDDFT calculations, which consistently predict that the $S_1$ state is an MLCT state (SI Chapter 6), and (iii) the absence of this band in the ligands (Fig. 4, SI Chapter 6 and Fig. S8.2).

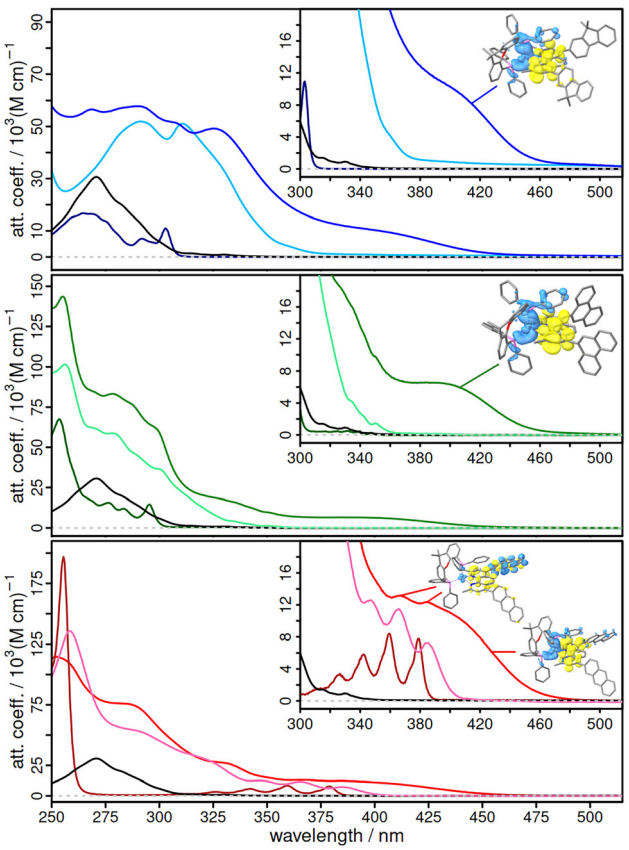


Fig. 4 UV/vis absorption spectra of **CunF** (top), **CunP** (middle), and **CunA** (bottom) compared to their individual fragments. Top: **CunF** (blue), **nF** (light blue), **neo** (black), **F** (dark blue). Middle: **CunP** (green), **nP** (light green), **neo** (black), **P** (dark green). Bottom: **CunA** (red), **nA** (light red), **neo** (black), **A** (dark red). Difference density plots in the top right of the insets show the migration of the electron density from blue (–) to yellow (+) during the MLCT excitations ($S_1 \leftarrow S_0$). An additional anthracene-localized $\pi_A^*–\pi_A$ excitation ($S_8 \leftarrow S_0$) is shown for **CunA**.

**Table 3** Experimental absorption wavelengths $\lambda_{abs,exp}$ (nm), extinction coefficients $\varepsilon$ ($10^3$ $M^{-1}cm^{-1}$), emission wavelengths $\lambda_{em,exp}$ (nm), emission quantum yields $\Phi_{em,exp}$ (%), emission lifetime $\tau_{em,exp}$ (μs), transient absorption lifetime $\tau_{tA,exp}$ (μs), compared to calculated fluorescence wavelengths $\lambda_{fl,calc}$ (relaxed $S_1$ → unrelaxed $S_0$, TDDFT) and phosphorescence wavelengths (relaxed $T_1$ → unrelaxed $S_0$, DFT) $\lambda_{ph,calc}$. All measurements were carried out in dichloromethane under inert conditions at 298 K. Computations were performed with implicit dichloromethane. The singlet–triplet energy gap $\Delta E_{S1-T1,calc}$ (eV) and interplane angles ($\theta$, °) of the optimized singlet $S_1$ and triplet $T_1$ are given. Optimization of the $S_1$ state in **CunA** yielded two different excited states depending on the sophistication of the method (see computational details). The first and lowest one is the $^1$MLCT and the second one was a $^1\pi_A$–$\pi_A^*$. The latter ended up as $S_2$ after convergence. Experimental data for **Cubcp** referenced from ref. 92

| | $\lambda_{abs}$/nm ($\varepsilon$/$10^3$ $M^{-1}$ $cm^{-1}$) | $\lambda_{em,exp.}$/nm | $\Phi_{em,exp.}$/% | $\tau_{em,exp.}$/ μs | $\tau_{tA,exp.}$/ μs | $\lambda_{fl,calc.}$/nm | $\lambda_{ph,calc.}$/ nm | $\Delta E_{S1-T1,calc.}$/ eV | $S_1$ $\theta_{calc.}$/ ° | $T_1$ $\theta_{calc.}$/ ° |
|---|---|---|---|---|---|---|---|---|---|---|
| **Cuneo** | 276 (47.4), 400 (3.29) | 559 | 27.9 | 7.04 | 6.51 | 599.4 | 741.9 | 0.388 | 70.1 | 70.4 |
| **Cubcp** | 287(59.8), 400(5.58) | 568 | 38.0 (ref. 92) | 8.38 | 8.04 | 580.3 | 756.2 | 0.404 | 74.3 | 71.0 |
| **CunF** | 269(56.6), 290(57.7) 325(49.2), 400 (10.3) | 570 | 44.2 | 20.78 | 21.62 | 576.9 | 745.5 | 0.385 | 73.7 | 71.6 |
| **CunP** | 255(143.6), 278(83.2) 325 (18.9), 400 (6.32) | 564 | 28.1 | 9.74 | 8.82 | 600.0 | 752.5 | 0.384 | 70.4 | 70.7 |
| **CunA** | 252(114.6), 285(75.8) 335(24.6), 400 (11.1) | 442 | 0.4 | n.d. | 37.28 174.36 | 608.0/ 476.5 | 866.6 | 0.722/1.036 | 75.5/ 82.8 | 83.8 |

As expected, **Cuneo** has the weakest MLCT absorption (Table 3), followed by **Cubcp**.[87,93] **CunP** exhibits a similar enhancement, suggesting that phenanthrene has a comparable influence to phenyl. In contrast, **CunF** and **CunA** both possess significantly higher attenuation coefficients.

TDDFT-derived difference densities confirm for all complexes that the lowest MLCT excitations (states 1–4, except **CunA**: 1, 4, 7, 11) have negligible substituent contribution (SI Chapter 6), consistent with the minimal red-shift. This indicates that the MLCT transitions are localized on the Cu(I)/diimine core, electronically decoupled from the substituents.[15,81] A comparable trend can be seen for the oscillator strength of the $S_1 \leftarrow S_0$ transition, suggesting that enhanced absorptivity stems from the elongated diimine system and a larger transition dipole moment.[75]

In the UV region (250–350 nm), the absorption is dominated by $\pi^* \leftarrow \pi$ transitions within the diimine ligand and the substituents.[29,71,87,90,91] **Cuneo** and **Cubcp** exhibit typical ligand-centered $\pi_{neo}^* \leftarrow \pi_{neo}$ transitions, corroborated by TDDFT (Fig. S6.2, S6.4, S6.13 and S6.15) and fragment spectrum (Fig. S8.4). Additional excitations involving xantphos and nonbonding MOs are present, but not discussed further.

Introducing PAH chromophores significantly alters the band shape and increases absorption (Fig. 4). A new shoulder at 300–350 nm appears experimentally (Fig. 4 and S8.5–8.7) and computationally (SI Chapter 6).

For **nP** and **CunP**, TDDFT indicates intraligand charge transfer (ILCT) from **P** to **neo** (Fig. S6.8 transition 2 and Fig. S6.19 transitions 5,6) and an enhancement of the weak $S_1 \leftarrow S_0$ transition in **P** and **neo** (Fig. S6.8 state 1 *vs.* S6.2 state 3). The MLCT transitions remain centered on the core complex, supporting an electronic decoupling of the two chromophores.

A similar observation is made for **nF** and **CunF**: between 250–350 nm, strong deviations from the fragments **F** and **neo** occur (Fig. 4 or S8.5). TDDFT reveals enhanced $\pi_{neo}^* \leftarrow \pi_{neo}$ transitions (Fig. S6.6 states 1,2) and strong ILCT transitions from **F** to **neo** ($\pi_{neo}^* \leftarrow \pi_F$, see Fig. S6.17 states 5–8,10). The bands at ≈290 and ≈310 nm in **CunF** and **nF** likely reflect fluorene-specific transitions, though an unambiguous assignment is not possible. Electronic communication between **neo** and **F** is somewhat stronger than in **CunP**, but a continuous π-system is still not formed.

For **CunA**, a subtle but distinct set of features is found: the MLCT band has two overlapping maxima at 385 and 366 nm. These are also present in **nA** and are attributed to vibronically structured anthracene-centered $\pi_A^* \leftarrow \pi_A$ transitions (Fig. 4 and S6.10 states 1,2). Additional transitions near the MLCT region display mixed local ($\pi_A^* \leftarrow \pi_A$) and charge transfer ($\pi_{neo}^* \leftarrow \pi_A$) character (S6.21 states 2, 3, 5, 6). Similar to the other systems, no significant red-shift of the MLCT band is observed, indicating negligible anthracene participation in the MLCT excitations. In the 300–350 nm range, however, **CunA** and **nA** display similar ILCT/π–π* patterns, suggesting an electronic communication between **neo** and **A** comparable to **CunF**.

## Emission behavior

The ligands **neo**, **bcp**, **nF**, **nP** and **nA** emit broadly in the 350 to 500 nm range (Fig. S9.1–3) and their quantum yields (*vs.* pyrene[93]) follow the order: **nA** (428 nm, $\phi_{em}$ = 46.4%) > **nF** (396 nm; $\phi_{em}$ = 29.6%) > **nP** (379 nm; $\phi_{em}$ = 6.2%) > **bcp** (385 nm; $\phi_{em}$ = 4.6%) > **neo** (364 nm; $\phi_{em}$ = 0.7%).

Upon excitation of the MLCT band at 390 nm, all complexes except **CunA** display yellow MLCT emission with a typically broad and featureless peak around 565 nm in deaerated dichloromethane (Fig. 5) as has been reported for **Cuneo**[87] and **Cubcp**.[11,29,76] **CunF** and **CunP** possess nearly identical emission wavelengths and band shapes compared to the references, differing mainly in emission intensity and quantum yield (referenced *vs.* **Cubcp**).[92] The quantum yield $\phi_{em}$ order is: **CunF** (44.2%) > **Cubcp** (38.0%[92]) > **CunP** (28.1%) ≈ **Cuneo** (27.9%, Table 3). A plausible explanation for this order combines different torsions (reduced overlap for **CunP**) with increased substituent rigidity in **CunF** (fluorene bridge), which disfavors non-radiative decay. Moreover, **CunF** exceeds **Cubcp**

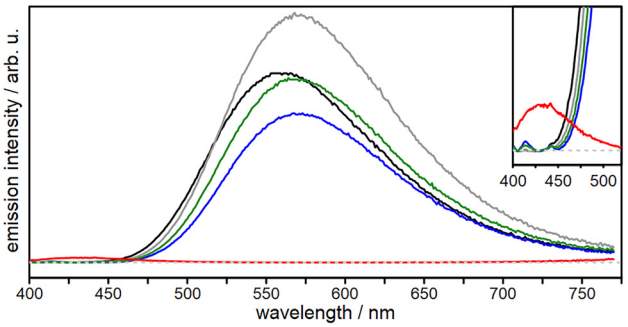


**Fig. 5** Emission spectra of **Cuneo** (black), **Cubcp** (gray), **CunF** (blue), **CunP** (green) and **CunA** (red) at excitation wavelength of 390 nm in deaerated dichloromethane. Samples were excited at an optical density of 0.1.

possibly due to the additional phenyl ring, which is forced in plane by the dimethylmethylene bridge.

Time-resolved emission (SI Chapter 10) gives lifetimes of 8.38 μs for **Cubcp** (*cf.* 7.24 μs, Forero-Cortés *et al.*[92]), 7.08 μs for **Cuneo**, 9.70 μs for **CunP**, indicating a negligible effect, and a significantly longer lifetime of 20.78 μs for **CunF**. Nevertheless, it is assumed that the final emissive state has MLCT characteristics, because the emission wavelength and shape are comparable to the references. Furthermore, computations reinforce a $^1$MLCT assignment (Table 3): (i) TDDFT-optimized $S_1$ states converged to the flattened $^1$MLCT state with fluorescence wavelengths closely matching experimentally observed values (Table 3); (ii) DFT-optimized $T_1$ states also converged to the flattened MLCT state, but the calculated phosphorescence wavelengths are strongly red-shifted due to underestimated triplet energies, which can be seen in the large calculated singlet–triplet gaps $\Delta E_{S1-T1}$ (>0.3 eV, Table 3).[3,29,87,91,94,95] Lastly, both singlet $S_1$ and triplet $T_1$ geometries demonstrate the characteristic MLCT flattening, where the interplane angle $\theta$ decreases from ≈86° to ≈72° on average (Table S5.2 and S5.3).[29]

In **CunA** the $^1$MLCT emission is absent and only a very weak band at 442 nm ($\Phi_{em}$ < 1%) attributed to the **nA** ligand is detected under deaerated conditions. TDDFT indicates two closely spaced singlet manifolds, a $d_{Cu}$–$\pi_{neo}$* $^1$MLCT state and an anthracene-localized $^1\pi_A$–$\pi_A$* state, whereby both can be obtained. The MLCT state yielded a theoretical emission wavelength of 608.0 nm with similar flattening of θ, while the anthracene-localized state yielded 476.5 nm with no geometric distortions to the Cu(I) core. Triplet–state ΔSCF optimizations reveal an anthracene-centered $^3\pi_A$–$\pi_A$* level lying well below the $^3$MLCT manifold, creating an energetically favorable, non-emissive energy sink. This enables efficient triplet–triplet energy transfer from the $^3$MLCT state, thereby quenching the $^1$MLCT emission and explaining its absence in **CunA**. Alternatively, the closely-spaced $^1\pi_A$–$\pi_A$* state may benefit from increased spin–orbit-coupling because of the Cu(I) chromophore to populate $^3\pi_A$–$\pi_A$* levels more easily.

To sum it up, the emission data establish a clear structure–property relationship: 9,9-dimethyl-9*H*-fluorene and phenanthrene substitution retain bright, long-lived MLCT emission, whereas anthracene diverts excitation into a low-lying, non-radiative triplet. This provides a practical design guideline: choose **F**/**P** substituents to retain a long-lived MLCT excited state with high radiative yield, and **A** when efficient triplet generation/storage is sought.

### Photostability and transient absorption spectroscopy

Prolonged irradiation with an intense, UV-rich light source (*e.g.* a 150 W Xe arc) facilitates a slow, steady photodecomposition (Fig. S12.1–S12.10). Both complexes and ligands in dichloromethane yield the same emissive photoproducts (Fig. S12.11, $\lambda_{em}$ = 488 nm for **Cuneo**; 444 nm for **Cubcp**; 508 nm for **CunF**; 520 nm for **CunP**; 617 nm for **CunA**). This suggests transformations within the diimine ligand rather than the Cu/xantphos fragment. Two non-exclusive hypotheses are consistent with literature: (i) light-induced dimerization/oligomerization enlarging the π-system (reported for bcp dimers with green fluorescence),[96,97] or (ii) reactions with radicals generated from chlorinated solvents.[98,99]

The transient absorption (tA, 355 nm pump) of **Cuneo** and **Cubcp** are characterized by very broad peaks around 521 and 534 nm (Fig. 6) with tA lifetimes ($\tau_{tA}$) of 6.51 μs and 8.04 μs, respectively. These lifetimes are monoexponential and comparable to the emissive lifetime. The tA spectrum has been attributed to the triplet–triplet absorption of the $^3$MLCT state, which matches the spin density of the lowest computed triplet (Fig. S6.23) and the computed triplet–triplet absorption spectrum (Fig. S6.24).[16,65] The band at about 525 nm is characterized by two excitation types, namely one local $\pi_{neo}$* ← $\pi_{neo}$ transition and ligand-to-metal charge transfers reducing the formal Cu(II) center (Fig. S6.24).

The PAH chromophore **F** could not be excited with 355 nm, but according to literature data of its derivative, 9*H*-fluorene has one sharp characteristic triplet–triplet absorption peak at around 375–390 nm.[100] However, the tA spectrum of **CunF** (Fig. 6) displays a broad maximum at 645 nm with a shoulder at 460 nm, which do not match the fluorene signature. Instead, the computed triplet–triplet spectrum of the $^3$MLCT state fits the spectral signature (Fig. S6.25). Compared to the reference complexes, the $^3$MLCT tA lifetime is effectively doubled to 21.62 μs with a new spectral signature.

The tA spectroscopy of **P** reveals two distinct peaks at 460 and 492 nm with a shoulder at 432 nm[100] (Fig. S11.1). **CunP** ($\tau_{tA}$ = 8.82 μs), however, does not display these peaks and exhibits a similar spectral signature (Fig. 6) as **Cuneo** and **Cubcp** with one broad feature at ≈508 nm and another at around 700 nm. This, together with the matching computed $^3$MLCT-triplet absorption (SI Fig. S6.25), suggests that the triplet state of **P** is not populated. This is reasonable as the $^3$MLCT is energetically lower than the triplet states of **P** and **F**.[101–103]

**A** also possesses two sharp characteristic triplet–triplet absorption bands at roughly 404 and 428 nm.[100] In contrast to both **CunF** and **CunP**, these characteristic peaks can also be found slightly shifted within **CunA** at 415 nm and 437 nm (Fig. 6 and S11.2). Furthermore, the tA spectrum of **CunA**

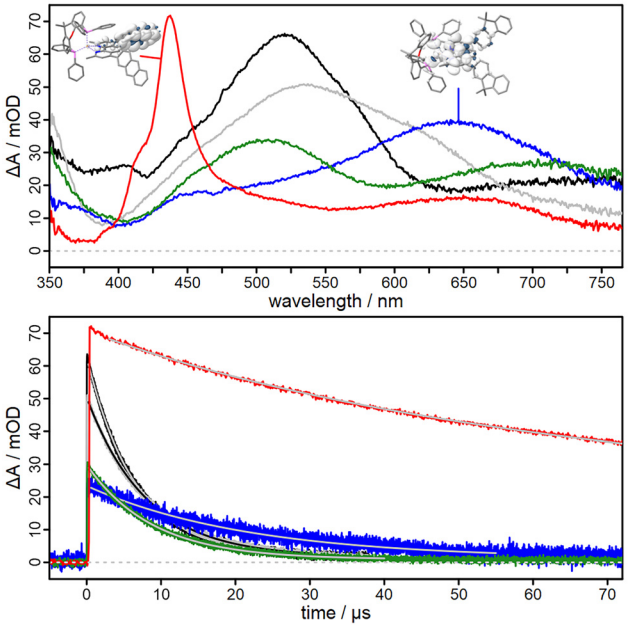


**Fig. 6** Nanosecond transient absorption spectra (top) of **Cuneo** (black), **Cubcp** (gray), **CunF** (blue), **CunP** (green) and **CunA** (red) in deaerated dichloromethane approximately 10 ns after excitation at 355 nm (absorbance of ≈0.3) with a detection gate-width of 3 μs. The decay kinetics (bottom) have been recorded at the transient absorption maxima: **Cuneo** (black, 521 nm), **Cubcp** (gray, 530 nm), **CunF** (blue, 645 nm), **CunP** (green, 505 nm) and **CunA** (red, 436 nm). See Fig S11.2 for full details on **CunA**. All complexes with the exception of **CunA** display a broad featureless transient spectrum that is attributed to the $^3$MLCT absorption and a representative spin density of the $^3$MLCT state of **CunF** is shown. **CunA** exhibits a sharp peak with a shoulder at 415 and 437 nm that is attributed to the absorption of the $^3\pi_A$–$\pi_A$* state of **A** as also shown by the spin density in the top left.[100]

agrees with the computed triplet–triplet absorption spectrum of the $^3\pi_A$–$\pi_A$* state (Fig. S6.26). This differentiates the PAH chromophores **F** and **P** from **A**, which efficiently funnels the excited state population into the low-lying anthracene-based $^3\pi_A$–$\pi_A$* $T_1$ state leading to vastly different photophysical properties. This is further evidenced in the significantly longer biexponential excited state lifetime ($\tau_{tA}$ = 37.28 and 174.36 μs).

In agreement with tA and the aforementioned findings (*i.e.* HOMO–LUMO gaps, electrochemistry, absorption and emission spectra) an energy level diagram of the novel complexes is proposed in Fig. S13.1 to illustrate possible photophysical decay pathways. To summarize, the lowest excited state in the four systems **Cuneo**, **Cubcp**, **CunF** and **CunP** has been identified to be of $^3$MLCT character. From a purely energetic perspective, the $^3\pi$–$\pi$* states of the substituents phenyl, **F** and **P** lie too high in energy in order to function as a triplet reservoir. Despite the latter, a significant extension of the lifetime has been observed for **CunF** which is about twice as large as in **Cubcp**, whereas that of **CunP** stayed similar to **Cuneo**. It is likely that this difference is attributed to geometric differences (*e.g.* more favorable dihedral angles). **CunA** on the other hand possesses very low-lying $^3\pi_A$–$\pi_A$* states that act as an energy sink, so that a repopulation of the $^3$MLCT state is no longer possible.

## Conclusions and outlook

In this study, three novel bichromophoric Cu(I) complexes **CunF**, **CunP**, and **CunA** were successfully synthesized and fully characterized. The diimine ligands are based on neocuproine (**neo**) and selectively functionalized at the 4,7-positions with polycyclic aromatic hydrocarbon chromophores – 9,9-dimethyl-9*H*-fluorene, phenanthrene, and anthracene. Structural analysis by X-ray diffraction (**CunA**) and DFT optimization confirms pseudo-tetrahedral geometries around the copper center. Due to steric hindrance, the attached organic chromophores adopt twisted, non-coplanar conformations relative to the diimine core. Electrochemical and spectroscopic analyses, supported by (TD-)DFT computations, evidence that the MLCT characteristics of the Cu(I) scaffold are largely retained for **CunF** and **CunP**, while **CunA** exhibits pronounced electronic mixing in the excited-state manifold. All complexes display strong MLCT absorption in the visible range with significantly increased molar attenuation coefficients compared to the references (**Cuneo** and **Cubcp**). **CunF** and **CunP** exhibit MLCT-based emission in the yellow region ($\lambda_{em}$ ≈ 565 nm) with quantum yields of 44.2% and 28.1%, respectively, and excited-state lifetimes up to 20.8 μs (**CunF**). In strong contrast, **CunA** has no detectable MLCT emission. Instead, a non-emissive, anthracene-localized $^3\pi_A$–$\pi_A$* state is populated, as confirmed by transient absorption spectroscopy and supported by TDDFT. Cyclic voltammetry revealed only moderate anodic shifts in the first reduction upon substitution with PAH chromophores. This indicates that the LUMO, at least for **CunF** and **CunP**, remains **neo**-centered and that the ground-state redox properties are largely preserved.

Three concise conclusions emerge: (i) structural torsion limits conjugation and preserves the Cu(I) redox core while increasing absorption strength; (ii) **CunF**/**CunP** retain MLCT excited states with long lifetimes, (iii) anthracene redirects the excited state into a low-lying, dark $^3\pi_A$–$\pi_A$* state that suppresses MLCT emission. Thus, substitution with PAH chromophores enables systematic tuning of absorption properties and excited-state dynamics without fundamentally altering the redox behavior, if the correct chromophore is chosen. **CunF** combines strong absorption, long lifetime and favorable redox potential, making it a promising candidate for photoredox catalysis. Similarly, **CunP**'s excited-state and redox properties compare directly to **Cuneo** and **Cubcp**, but with significantly stronger UV absorption. The unique photophysical behavior of **CunA** enabled by a very long-lived locally excited triplet state opens up perspectives for its application in energy transfer catalysis and photon upconversion, *e.g. via* triplet–triplet annihilation (TTA).

In future studies, both directions will be explored. Moreover, the modular approach of combining Cu(I)-MLCT chromophores with rigid, non-coplanar π-systems may be

 

extended to other platforms, offering a versatile strategy to design photoactive metal complexes with tailored excited-state landscapes.

## Conflicts of interest

The authors declare no competing financial interests.

## Data availability

The data supporting this article have been included as part of the supplementary information (SI). Supplementary information: additional experimental, synthetic, computational, spectroscopic and electrochemical details. See DOI: **https://doi.org/10.1039/d5qi02274f**.

CCDC 2491672 (**CunA**) contains the supplementary crystallographic data for this paper.[104]

## Acknowledgements

We are grateful to Cengiz Özmen (TU Braunschweig) for help with solvent purification. L. E. B. is thankful for a doctoral scholarship by the Deutsche Bundesstiftung Umwelt (DBU, AZ: 20024/029). J. P. Z. expresses gratitude to the Cusanuswerk e.V. for a doctoral scholarship.

## References

1 C. B. Larsen and O. S. Wenger, Photoredox Catalysis with Metal Complexes Made from Earth-Abundant Elements, *Chem. – Eur. J.*, 2018, **24**, 2039–2058.
2 C. Sandoval-Pauker, G. Molina-Aguirre and B. Pinter, Status report on copper(I) complexes in photoredox catalysis; photophysical and electrochemical properties and future prospects, *Polyhedron*, 2021, **199**, 115105.
3 J. Beaudelot, S. Oger, S. Peruško, T.-A. Phan, T. Teunens, C. Moucheron and G. Evano, Photoactive Copper Complexes: Properties and Applications, *Chem. Rev.*, 2022, **122**, 16365–16609.
4 C. E. Housecroft and E. C. Constable, The emergence of copper(I)-based dye sensitized solar cells, *Chem. Soc. Rev.*, 2015, **44**, 8386–8398.
5 A. Lennert and D. M. Guldi, Homoleptic and Heteroleptic Copper Complexes as Redox Couples in Dye-Sensitized Solar Cells, *ChemPhotoChem*, 2019, **3**, 636–644.
6 D. Franchi, V. Leandri, A. R. P. Pizzichetti, B. Xu, Y. Hao, W. Zhang, T. Sloboda, S. Svanström, U. B. Cappel, L. Kloo, L. Sun and J. M. Gardner, Effect of the Ancillary Ligand on the Performance of Heteroleptic Cu(I) Diimine Complexes as Dyes in Dye-Sensitized Solar Cells, *ACS Appl. Energy Mater.*, 2022, **5**, 1460–1470.
7 L. E. Burmeister, F. Doettinger, K. J. Haseloff, C. Kleeberg, M. Boujtita, S. Pascal, F. Odobel, S. Tschierlei, Y. Pellegrin and M. Karnahl, Dye-Sensitized Solar Cells Based on Cu(I) Complexes Containing Catechol Anchor Groups That Operate with Aqueous Electrolytes, *JACS Au*, 2025, **5**, 3960–3973.
8 Q. Zhang, J. Ding, Y. Cheng, L. Wang, Z. Xie, X. Jing and F. Wang, Novel Heteroleptic CuI Complexes with Tunable Emission Color for Efficient Phosphorescent Light-Emitting Diodes, *Adv. Funct. Mater.*, 2007, **17**, 2983–2990.
9 D. M. Zink, D. Volz, T. Baumann, M. Mydlak, H. Flügge, J. Friedrichs, M. Nieger and S. Bräse, Dinuclear Copper(I) Complexes for Application in Organic Light-Emitting Diodes, *Chem. Mater.*, 2013, **25**, 4471–4486.
10 S.-P. Luo, E. Mejía, A. Friedrich, A. Pazidis, H. Junge, A.-E. Surkus, R. Jackstell, S. Denurra, S. Gladiali, S. Lochbrunner and M. Beller, Photocatalytic Water Reduction with Copper-Based Photosensitizers: A Noble-Metal-Free System, *Angew. Chem., Int. Ed.*, 2013, **52**, 419–423.
11 E. Mejía, S.-P. Luo, M. Karnahl, A. Friedrich, S. Tschierlei, A.-E. Surkus, H. Junge, S. Gladiali, S. Lochbrunner and M. Beller, A Noble-Metal-Free System for Photocatalytic Hydrogen Production from Water, *Chem. – Eur. J.*, 2013, **19**, 15972–15978.
12 N.-Y. Chen, L.-M. Xia, A. J. J. Lennox, Y.-Y. Sun, H. Chen, H.-M. Jin, H. Junge, Q.-A. Wu, J.-H. Jia, M. Beller and S.-P. Luo, Structure-Activated Copper Photosensitisers for Photocatalytic Water Reduction, *Chem. – Eur. J.*, 2017, **23**, 3631–3636.
13 J. Kim, D. R. Whang and S. Y. Park, Designing Highly Efficient CuI Photosensitizers for Photocatalytic $H_2$ Evolution from Water, *ChemSusChem*, 2017, **10**, 1883–1886.
14 H. Takeda, H. Kamiyama, K. Okamoto, M. Irimajiri, T. Mizutani, K. Koike, A. Sekine and O. Ishitani, Highly Efficient and Robust Photocatalytic Systems for $CO_2$ Reduction Consisting of a Cu(I) Photosensitizer and Mn(I) Catalysts, *J. Am. Chem. Soc.*, 2018, **140**, 17241–17254.
15 H. Takeda, Y. Monma, H. Sugiyama, H. Uekusa and O. Ishitani, Development of Visible-Light Driven Cu(I) Complex Photosensitizers for Photocatalytic $CO_2$ Reduction, *Front. Chem.*, 2019, **7**, 418.
16 J.-W. Wang, X. Zhang, L. Velasco, M. Karnahl, Z. Li, Z.-M. Luo, Y. Huang, J. Yu, W. Hu, X. Zhang, K. Yamauchi, K. Sakai, D. Moonshiram and G. Ouyang, Precious-Metal-Free $CO_2$ Photoreduction Boosted by Dynamic Coordinative Interaction between Pyridine-Tethered Cu(I) Sensitizers and a Co(II) Catalyst, *JACS Au*, 2023, **3**, 1984–1997.
17 R. D. Costa, E. Ortí, H. J. Bolink, F. Monti, G. Accorsi and N. Armaroli, Luminescent Ionic Transition-Metal Complexes for Light-Emitting Electrochemical Cells, *Angew. Chem., Int. Ed.*, 2012, **51**, 8178–8211.
18 Y.-J. Yuan, Z.-T. Yu, D.-Q. Chen and Z.-G. Zou, Metal-complex chromophores for solar hydrogen generation, *Chem. Soc. Rev.*, 2017, **46**, 603–631.
19 T. Mede, M. Jäger and U. S. Schubert, "Chemistry-on-the-complex": functional RuII polypyridyl-type sensitizers as

divergent building blocks, *Chem. Soc. Rev.*, 2018, **47**, 7577–7627.

20 O. S. Wenger, Photoactive Complexes with Earth-Abundant Metals, *J. Am. Chem. Soc.*, 2018, **140**, 13522–13533.

21 B. M. Hockin, C. Li, N. Robertson and E. Zysman-Colman, Photoredox catalysts based on earth-abundant metal complexes, *Catal. Sci. Technol.*, 2019, **9**, 889–915.

22 S. Paria and O. Reiser, Copper in Photocatalysis, *ChemCatChem*, 2014, **6**, 2477–2483.

23 F. Doettinger, C. Kleeberg, C. Queffélec, S. Tschierlei, Y. Pellegrin and M. Karnahl, Rich or poor: the impact of electron donation and withdrawal on the photophysical and photocatalytic properties of copper(I) complexes, *Catal. Sci. Technol.*, 2023, **13**, 4092–4106.

24 S. Fischer, D. Hollmann, S. Tschierlei, M. Karnahl, N. Rockstroh, E. Barsch, P. Schwarzbach, S.-P. Luo, H. Junge, M. Beller, S. Lochbrunner, R. Ludwig and A. Brückner, Death and Rebirth: Photocatalytic Hydrogen Production by a Self-Organizing Copper–Iron System, *ACS Catal.*, 2014, **4**, 1845–1849.

25 H. Takeda, K. Ohashi, A. Sekine and O. Ishitani, Photocatalytic $CO_2$ Reduction Using Cu(I) Photosensitizers with a Fe(II) Catalyst, *J. Am. Chem. Soc.*, 2016, **138**, 4354–4357.

26 C. Steinlechner, A. F. Roesel, E. Oberem, A. Päpcke, N. Rockstroh, F. Gloaguen, S. Lochbrunner, R. Ludwig, A. Spannenberg, H. Junge, R. Francke and M. Beller, Selective Earth-Abundant System for $CO_2$ Reduction: Comparing Photo- and Electrocatalytic Processes, *ACS Catal.*, 2019, **9**, 2091–2100.

27 X. Zhang, M. Cibian, A. Call, K. Yamauchi and K. Sakai, Photochemical $CO_2$ Reduction Driven by Water-Soluble Copper(I) Photosensitizer with the Catalysis Accelerated by Multi-Electron Chargeable Cobalt Porphyrin, *ACS Catal.*, 2019, **9**, 11263–11273.

28 G. Accorsi, A. Listorti, K. Yoosaf and N. Armaroli, 1,10-Phenanthrolines: versatile building blocks for luminescent molecules, materials and metal complexes, *Chem. Soc. Rev.*, 2009, **38**, 1690–1700.

29 Y. Zhang, M. Schulz, M. Wächtler, M. Karnahl and B. Dietzek, Heteroleptic diimine–diphosphine Cu(I) complexes as an alternative towards noble-metal based photosensitizers: Design strategies, photophysical properties and perspective applications, *Coord. Chem. Rev.*, 2018, **356**, 127–146.

30 P. A. Forero Cortés, M. Marx, M. Trose and M. Beller, Heteroleptic copper complexes with nitrogen and phosphorus ligands in photocatalysis: Overview and perspectives, *Chem. Catal.*, 2021, **1**, 298–338.

31 C. Weinheimer, Y. Choi, T. Caldwell, P. Gresham and J. Olmsted III, Effect of a steric spacer on chromophoric interactions of ruthenium complexes containing covalently bound anthracene, *J. Photochem. Photobiol., A*, 1994, **78**, 119–126.

32 G. J. Wilson, W. H. F. Sasse and A. W.-H. Mau, Singlet and triplet energy transfer processes in ruthenium(II) bipyridine complexes containing covalently bound arenes, *Chem. Phys. Lett.*, 1996, **250**, 583–588.

33 G. J. Wilson, A. Launikonis, W. H. F. Sasse and A. W.-H. Mau, Excited-State Processes in Ruthenium(II) Bipyridine Complexes Containing Covalently Bound Arenes, *J. Phys. Chem. A*, 1997, **101**, 4860–4866.

34 N. D. McClenaghan, Y. Leydet, B. Maubert, M. T. Indelli and S. Campagna, Excited-state equilibration: a process leading to long-lived metal-to-ligand charge transfer luminescence in supramolecular systems, *Coord. Chem. Rev.*, 2005, **249**, 1336–1350.

35 H. Li, C. Wang, F. Glaser, N. Sinha and O. S. Wenger, Metal-Organic Bichromophore Lowers the Upconversion Excitation Power Threshold and Promotes UV Photoreactions, *J. Am. Chem. Soc.*, 2023, **145**, 11402–11414.

36 F. N. Castellano, Altering Molecular Photophysics by Merging Organic and Inorganic Chromophores, *Acc. Chem. Res.*, 2015, **48**, 828–839.

37 M.-S. Bertrams, K. Hermainski, J.-M. Mörsdorf, J. Ballmann and C. Kerzig, Triplet quenching pathway control with molecular dyads enables the identification of a highly oxidizing annihilator class, *Chem. Sci.*, 2023, **14**, 8583–8591.

38 J. E. Yarnell, J. C. Deaton, C. E. McCusker and F. N. Castellano, Bidirectional "Ping-Pong" Energy Transfer and 3000-Fold Lifetime Enhancement in a Re(I) Charge Transfer Complex, *Inorg. Chem.*, 2011, **50**, 7820–7830.

39 N. Sinha, C. Wegeberg, D. Häussinger, A. Prescimone and O. S. Wenger, Photoredox-active Cr(0) luminophores featuring photophysical properties competitive with Ru(II) and Os(II) complexes, *Nat. Chem.*, 2023, **15**, 1730–1736.

40 F. N. Castellano and M. C. Rosko, Steric and Electronic Influence of Excited-State Decay in Cu(I) MLCT Chromophores, *Acc. Chem. Res.*, 2024, **57**, 2872–2886.

41 G. E. Shillito, C. B. Larsen, J. R. W. McLay, N. T. Lucas and K. C. Gordon, Effect of Bridge Alteration on Ground- and Excited-State Properties of Ruthenium(II) Complexes with Electron-Donor-Substituted Dipyrido[3,2-a:2′,3′-c]phenazine Ligands, *Inorg. Chem.*, 2016, **55**, 11170–11184.

42 P. Dierks, A. Päpcke, O. S. Bokareva, B. Altenburger, T. Reuter, K. Heinze, O. Kühn, S. Lochbrunner and M. Bauer, Ground- and Excited-State Properties of Iron(II) Complexes Linked to Organic Chromophores, *Inorg. Chem.*, 2020, **59**, 14746–14761.

43 S. Neumann, O. S. Wenger and C. Kerzig, Controlling Spin-Correlated Radical Pairs with Donor–Acceptor Dyads: A New Concept to Generate Reduced Metal Complexes for More Efficient Photocatalysis, *Chem. – Eur. J.*, 2021, **27**, 4115–4123.

44 G. E. Shillito, D. Preston, J. D. Crowley, P. Wagner, S. J. Harris, K. C. Gordon and S. Kupfer, Controlling Excited State Localization in Bichromophoric Photosensitizers via the Bridging Group, *Inorg. Chem.*, 2024, **63**, 4947–4956.

 

45 A. Lavie-Cambot, C. Lincheneau, M. Cantuel, Y. Leydet and N. D. McClenaghan, Reversible electronic energy transfer: a means to govern excited-state properties of supramolecular systems, *Chem. Soc. Rev.*, 2010, **39**, 506–515.
46 D. S. Tyson and F. N. Castellano, Intramolecular Singlet and Triplet Energy Transfer in a Ruthenium(II) Diimine Complex Containing Multiple Pyrenyl Chromophores, *J. Phys. Chem. A*, 1999, **103**, 10955–10960.
47 F. Odobel and H. Zabri, Preparations and Characterizations of Bichromophoric Systems Composed of a Ruthenium Polypyridine Complex Connected to a Difluoroborazaindacene or a Zinc Phthalocyanine Chromophore, *Inorg. Chem.*, 2005, **44**, 5600–5611.
48 F. Glaser, C. Kerzig and O. S. Wenger, Multi-Photon Excitation in Photoredox Catalysis: Concepts, Applications, Methods, *Angew. Chem., Int. Ed.*, 2020, **59**, 10266–10284.
49 D. M. Arias-Rotondo and J. K. McCusker, The photophysics of photoredox catalysis: a roadmap for catalyst design, *Chem. Soc. Rev.*, 2016, **45**, 5803–5820.
50 F. Doettinger, Y. Yang, M. Karnahl and S. Tschierlei, Bichromophoric Photosensitizers: How and Where to Attach Pyrene Moieties to Phenanthroline to Generate Copper(I) Complexes, *Inorg. Chem.*, 2023, **62**, 8166–8178.
51 M. Baba, Intersystem Crossing in the $^1n\pi^*$ and $^1\pi\pi^*$ States, *J. Phys. Chem. A*, 2011, **115**, 9514–9519.
52 A. J. Floyd, S. F. Dyke and S. E. Ward, The synthesis of phenanthrenes, *Chem. Rev.*, 1976, **76**, 509–562.
53 M. Yoshizawa and J. K. Klosterman, Molecular architectures of multi-anthracene assemblies, *Chem. Soc. Rev.*, 2014, **43**, 1885–1898.
54 V. Gray, D. Dzebo, A. Lundin, J. Alborzpour, M. Abrahamsson, B. Albinsson and K. Moth-Poulsen, Photophysical characterization of the 9,10-disubstituted anthracene chromophore and its applications in triplet–triplet annihilation photon upconversion, *J. Mater. Chem. C*, 2015, **3**, 11111–11121.
55 J. Shaya, F. Fontaine-Vive, B. Y. Michel and A. Burger, Rational Design of Push–Pull Fluorene Dyes: Synthesis and Structure-Photophysics Relationship, *Chem. – Eur. J.*, 2016, **22**, 10627–10637.
56 G. S. Baviera and P. M. Donate, Recent advances in the syntheses of anthracene derivatives, *Beilstein J. Org. Chem.*, 2021, **17**, 2028–2050.
57 A. Olesund, V. Gray, J. Mårtensson and B. Albinsson, Diphenylanthracene Dimers for Triplet–Triplet Annihilation Photon Upconversion: Mechanistic Insights for Intramolecular Pathways and the Importance of Molecular Geometry, *J. Am. Chem. Soc.*, 2021, **143**, 5745–5754.
58 J. Shaya, P. R. Corridon, B. Al-Omari, A. Aoudi, A. Shunnar, M. I. H. Mohideen, A. Qurashi, B. Y. Michel and A. Burger, Design, photophysical properties, and applications of fluorene-based fluorophores in two-photon fluorescence bioimaging: A review, *J. Photochem. Photobiol., C*, 2022, **52**, 100529.
59 K. D. Belfield, M. V. Bondar, C. O. Yanez, F. E. Hernandez and O. V. Przhonska, Two-photon absorption and lasing properties of new fluorene derivatives, *J. Mater. Chem.*, 2009, **19**, 7498–7502.
60 K. Lim, C. Kim, J. Song, T. Yu, W. Lim, K. Song, P. Wang, N. Zu and J. Ko, Enhancing the Performance of Organic Dye-Sensitized Solar Cells via a Slight Structure Modification, *J. Phys. Chem. C*, 2011, **115**, 22640–22646.
61 M. Pawlicki, H. A. Collins, R. G. Denning and H. L. Anderson, Two-Photon Absorption and the Design of Two-Photon Dyes, *Angew. Chem., Int. Ed.*, 2009, **48**, 3244–3266.
62 T. N. Singh-Rachford and F. N. Castellano, Photon upconversion based on sensitized triplet-triplet annihilation, *Coord. Chem. Rev.*, 2010, **254**, 2560–2573.
63 F. Deng, J. Blumhoff and F. N. Castellano, Annihilation Limit of a Visible-to-UV Photon Upconversion Composition Ascertained from Transient Absorption Kinetics, *J. Phys. Chem. A*, 2013, **117**, 4412–4419.
64 A. Suzuki, Carbon-carbon bonding made easy, *Chem. Commun.*, 2005, 4759–4763.
65 F. Doettinger, Y. Yang, M.-A. Schmid, W. Frey, M. Karnahl and S. Tschierlei, Cross-Coupled Phenyl- and Alkynyl-Based Phenanthrolines and Their Effect on the Photophysical and Electrochemical Properties of Heteroleptic Cu(I) Photosensitizers, *Inorg. Chem.*, 2021, **60**, 5391–5401.
66 J. E. Nycz, J. Wantulok, R. Sokolova, L. Pajchel, M. Stankevič, M. Szala, J. G. Malecki and D. Swoboda, Synthesis and Electrochemical and Spectroscopic Characterization of 4,7-diamino-1,10-phenanthrolines and Their Precursors, *Molecules*, 2019, **24**, 4102.
67 T. Kinzel, Y. Zhang and S. L. Buchwald, A New Palladium Precatalyst Allows for the Fast Suzuki–Miyaura Coupling Reactions of Unstable Polyfluorophenyl and 2-Heteroaryl Boronic Acids, *J. Am. Chem. Soc.*, 2010, **132**, 14073–14075.
68 Y. Zhang, M. Heberle, M. Wächtler, M. Karnahl and B. Dietzek, Determination of side products in the photocatalytic generation of hydrogen with copper photosensitizers by resonance Raman spectroelectrochemistry, *RSC Adv.*, 2016, **6**, 105801–105805.
69 M. Heberle, S. Tschierlei, N. Rockstroh, M. Ringenberg, W. Frey, H. Junge, M. Beller, S. Lochbrunner and M. Karnahl, Heteroleptic Copper Photosensitizers: Why an Extended π-System Does Not Automatically Lead to Enhanced Hydrogen Production, *Chem. – Eur. J.*, 2017, **23**, 312–319.
70 M. S. Lazorski and F. N. Castellano, Advances in the light conversion properties of Cu(I)-based photosensitizers, *Polyhedron*, 2014, **82**, 57–70.
71 M. Sandroni, Y. Pellegrin and F. Odobel, Heteroleptic bis-diimine copper(I) complexes for applications in solar energy conversion, *C. R. Chim.*, 2016, **19**, 79–93.
72 V. Leandri, A. R. P. Pizzichetti, B. Xu, D. Franchi, W. Zhang, I. Benesperi, M. Freitag, L. Sun, L. Kloo and J. M. Gardner, Exploring the Optical and Electrochemical

Properties of Homoleptic versus Heteroleptic Diimine Copper(I) Complexes, *Inorg. Chem.*, 2019, **58**, 12167–12177.

73 J. Beaudelot, G. Evano and C. Moucheron, Structure-Property Relationships in a New Family of Photoactive Diimine-Diphosphine Copper(I) Complexes, *Chem. – Eur. J.*, 2023, **29**, e202300758.

74 J. R. Kirchhoff, D. R. McMillin, W. R. Robinson, D. R. Powell, A. T. McKenzie and S. Chen, Steric effects and the behavior of $Cu(NN)(PPh_3)_2^+$ systems in fluid solution. Crystal and molecular structures of $[Cu(dmp)(PPh_3)_2]NO_3$ and $[Cu(phen)(PPh_3)_2]NO_3{\cdot}1.5EtOH$, *Inorg. Chem.*, 1985, **24**, 3928–3933.

75 T. Tsubomura, K. Kimura, M. Nishikawa and T. Tsukuda, Structures and photophysical properties of copper(I) complexes bearing diphenylphenanthroline and bis(diphenylphosphino)alkane: the effect of phenyl groups on the phenanthroline ligand, *Dalton Trans.*, 2015, **44**, 7554–7562.

76 D. Moonshiram, P. Garrido-Barros, C. Gimbert-Suriñach, A. Picón, C. Liu, X. Zhang, M. Karnahl and A. Llobet, Elucidating the Nature of the Excited State of a Heteroleptic Copper Photosensitizer by using Time-Resolved X-ray Absorption Spectroscopy, *Chem. – Eur. J.*, 2018, **24**, 6464–6472.

77 F. Grein, Twist Angles and Rotational Energy Barriers of Biphenyl and Substituted Biphenyls, *J. Phys. Chem. A*, 2002, **106**, 3823–3827.

78 B. Milián-Medina and J. Gierschner, π-Conjugation, *Wiley Interdiscip. Rev.: Comput. Mol. Sci.*, 2012, **2**, 513–524.

79 J. Jia, H.-S. Wu, Z. Chen and Y. Mo, Elucidation of the Forces Governing the Stereochemistry of Biphenyl, *Eur. J. Org. Chem.*, 2013, 611–616.

80 B. Landeros-Rivera and J. Hernández-Trujillo, Control of Molecular Conformation and Crystal Packing of Biphenyl Derivatives, *ChemPlusChem*, 2022, **87**, e202100492.

81 H. Takeda, M. Shimo, G. Yasuhara, K. Kobori, M. S. Asano and Y. Amao, Heteroleptic Cu(I) Phenanthroline Complexes Bearing Benzoxazole and Benzothiazole Moieties for Visible Light Absorption, *Chem. Lett.*, 2021, **51**, 69–72.

82 M. Iwamura, S. Takeuchi and T. Tahara, Ultrafast Excited-State Dynamics of Copper(I) Complexes, *Acc. Chem. Res.*, 2015, **48**, 782–791.

83 C. Li, R. Dickson, N. Rockstroh, J. Rabeah, D. B. Cordes, A. M. Z. Slawin, P. Hünemörder, A. Spannenberg, M. Bühl, E. Mejía, E. Zysman-Colman and P. C. J. Kamer, Ligand electronic fine-tuning and its repercussion on the photocatalytic activity and mechanistic pathways of the copper-photocatalysed aza-Henry reaction, *Catal. Sci. Technol.*, 2020, **10**, 7745–7756.

84 Y. Yamazaki, T. Onoda, J. Ishikawa, S. Furukawa, C. Tanaka, T. Utsugi and T. Tsubomura, Photocatalytic $CO_2$ Reduction Using Various Heteroleptic Diimine-Diphosphine Cu(I) Complexes as Photosensitizers, *Front. Chem.*, 2019, **7**, 288.

85 Z.-J. Yu, H. Chen, A. J. Lennox, L.-J. Yan, X.-F. Liu, D.-D. Xu, F. Chen, L.-X. Xu, Y. Li, Q.-A. Wu and S.-P. Luo, Heteroleptic copper(I) photosensitizers with carbazole-substituted phenanthroline ligands: Synthesis, photophysical properties and application to photocatalytic $H_2$ generation, *Dyes Pigm.*, 2019, **162**, 771–775.

86 A. Kaeser, M. Mohankumar, J. Mohanraj, F. Monti, M. Holler, J.-J. Cid, O. Moudam, I. Nierengarten, L. Karmazin-Brelot, C. Duhayon, B. Delavaux-Nicot, N. Armaroli and J.-F. Nierengarten, Heteroleptic Copper(I) Complexes Prepared from Phenanthroline and Bis-Phosphine Ligands, *Inorg. Chem.*, 2013, **52**, 12140–12151.

87 C. Li, C. F. R. Mackenzie, S. A. Said, A. K. Pal, M. A. Haghighatbin, A. Babaei, M. Sessolo, D. B. Cordes, A. M. Z. Slawin, P. C. J. Kamer, H. J. Bolink, C. F. Hogan and E. Zysman-Colman, Wide-Bite-Angle Diphosphine Ligands in Thermally Activated Delayed Fluorescent Copper(I) Complexes: Impact on the Performance of Electroluminescence Applications, *Inorg. Chem.*, 2021, **60**, 10323–10339.

88 M. Rentschler, M.-A. Schmid, W. Frey, S. Tschierlei and M. Karnahl, Multidentate Phenanthroline Ligands Containing Additional Donor Moieties and Their Resulting Cu(I) and Ru(II) Photosensitizers: A Comparative Study, *Inorg. Chem.*, 2020, **59**, 14762–14771.

89 F. Doettinger, M. Obermeier, V. Caliskanyürek, L. E. Burmeister, C. Kleeberg, M. Karnahl, M. Schwalbe and S. Tschierlei, Bright or Dark: Unexpected Photocatalytic Behavior of Closely Related Phenanthroline-based Copper(I) Photosensitizers, *ChemCatChem*, 2023, **15**, e202300452.

90 N. Armaroli, Photoactive mono- and polynuclear Cu(I)–phenanthrolines. A viable alternative to Ru(I)–polypyridines?, *Chem. Soc. Rev.*, 2001, **30**, 113–124.

91 C. Sandoval-Pauker, M. Santander-Nelli and P. Dreyse, Thermally activated delayed fluorescence in luminescent cationic copper(I) complexes, *RSC Adv.*, 2022, **12**, 10653–10674.

92 P. A. Forero-Cortés, M. Marx, N. G. Moustakas, F. Brunner, C. E. Housecroft, E. C. Constable, H. Junge, M. Beller and J. Strunk, Transferring photocatalytic $CO_2$ reduction mediated by $Cu(N\hat{}N)(P\hat{}P)^+$ complexes from organic solvents into ionic liquid media, *Green Chem.*, 2020, **22**, 4541–4549.

93 D. S. Karpovich and G. J. Blanchard, Relating the polarity-dependent fluorescence response of pyrene to vibronic coupling. Achieving a fundamental understanding of the py polarity scale, *J. Phys. Chem.*, 1995, **99**, 3951–3958.

94 M. R. Silva-Junior, M. Schreiber, S. P. A. Sauer and W. Thiel, Benchmarks for electronically excited states: Time-dependent density functional theory and density functional theory based multireference configuration interaction, *J. Chem. Phys.*, 2008, **129**, 104103.

95 R. Grotjahn, T. M. Maier, J. Michl and M. Kaupp, Development of a TDDFT-Based Protocol with Local Hybrid Functionals for the Screening of Potential Singlet

 

Fission Chromophores, *J. Chem. Theory Comput.*, 2017, **13**, 4984–4996.

96 S. Scholz, C. Corten, K. Walzer, D. Kuckling and K. Leo, Photochemical reactions in organic semiconductor thin films, *Org. Electron.*, 2007, **8**, 709–717.

97 M. Miśnik, K. Falkowski, W. Mróz and W. Stampor, Electromodulation of photoluminescence in vacuum-evaporated films of bathocuproine, *Chem. Phys.*, 2013, **410**, 45–54.

98 S. Yamada, H. Kuroki, M. Maeda, M. Takagi and T. Yamashita, Characterization of Pyrene Photoproducts in Chloroform by Gas-Chromatography and Gas-Chromatography Mass-Spectrometry, *Microchem. J.*, 1994, **49**, 117–125.

99 J. Aguilera-Sigalat, J. Sanchez-SanMartín, C. E. Agudelo-Morales, E. Zaballos, R. E. Galian and J. Pérez-Prieto, Further Insight into the Photostability of the Pyrene Fluorophore in Halogenated Solvents, *ChemPhysChem*, 2012, **13**, 835–844.

100 I. Carmichael and G. L. Hug, Triplet–Triplet Absorption Spectra of Organic Molecules in Condensed Phases, *J. Phys. Chem. Ref. Data*, 1986, **15**, 1–250.

101 D. S. McClure, Triplet-Singlet Transitions in Organic Molecules. Lifetime Measurements of the Triplet State, *J. Chem. Phys.*, 1949, **17**, 905–913.

102 J. Langelaar, R. P. H. Rettschnick and G. J. Hoijtink, Studies on Triplet Radiative Lifetimes, Phosphorescence, and Delayed Fluorescence Yields of Aromatic Hydrocarbons in Liquid Solutions, *J. Chem. Phys.*, 1971, **54**, 1–7.

103 S. Scypinski and L. J. C. Love, Room-temperature phosphorescence of polynuclear aromatic hydrocarbons in cyclodextrins, *Anal. Chem.*, 1984, **56**, 322–327.

104 CCDC 2491672: Experimental Crystal Structure Determination, 2026, DOI: **10.5517/ccdc.csd.cc2pmsjn**.